Published in final edited form as:

Magn Reson Imaging. 2017 October ; 42: 158–163. doi:10.1016/j.mri.2017.07.019.

Large improvement of RF transmission efficiency and reception sensitivity for human *in vivo* ^{31}P MRS imaging using ultrahigh dielectric constant materials at 7 T

Byeong-Yeul Lee[a], **Xiao-Hong Zhu**[a], **Sebastian Rupprecht**[b], **Michael T. Lanagan**[c], **Qing X. Yang**[b,*], and **Wei Chen**[a,*]

[a]Center for Magnetic Resonance Research, Department of Radiology, University of Minnesota Medical School, MN, USA

[b]Center for NMR Research, Department of Radiology, Pennsylvania State College of Medicine, Hershey, PA, USA

[c]Department of Engineering Science and Mechanics, The Pennsylvania State College of Engineering, University Park, PA, USA

Abstract

In vivo ^{31}P MRS provides a unique and important imaging tool for studying high-energy phosphate metabolism and bioenergetics noninvasively. However, compared to ^{1}H MRS, ^{31}P MRS with a relatively low gyromagnetic ratio (γ) has a lower and limited sensitivity even at ultrahigh field. The proof of concept has been recently demonstrated that the use of high dielectric constant (HDC) materials between RF coil and object sample could increase MRI signal and reduce required RF transmission power for reaching the same RF pulse flip angle in the region of interest. For low-γ MRS applications operated at relatively lower frequency, however, it demands the dielectric materials with a much higher permittivity for achieving optimal performance. We conducted a ^{31}P MRS imaging study using ultra-HDC (uHDC; with a relative permittivity of ~1200) material blocks incorporated with an RF volume coil at ultrahigh field of 7.0 T. The experimental results from phantom and human calf muscle demonstrate that the uHDC technique significantly enhanced RF magnetic transmit field (B_1^+) and reception field (B_1^-) and the gain could reach up to two folds in the tissue near the uHDC blocks. The overall results indicate that the incorporation of the uHDC materials having an appropriate permittivity value with a RF coil can significantly increase detection sensitivity and reduces RF transmission power for X-nuclei MRS applications at ultrahigh field. The uHDC technology could provide an efficient, cost-effective engineering solution for achieving high detection sensitivity and concurrently minimizing tissue heating concern for human MRS and MRI applications.

*Corresponding authors at: Center for Magnetic Resonance Research (CMRR), University of Minnesota, 2021 6th St. SE, Minneapolis, MN 55455, USA. qyang@psu.edu (Q.X. Yang), wei@cmrr.umn.edu (W. Chen).

Disclosure

Qing X. Yang, Sebastian Rupprecht and Michael T, Lanagan are affiliated with HyQ Research Solutions, LLC, State College, PA.

Keywords

^{31}P MRS; B_1 magnetic field; Ultrahigh dielectric constant material; RF transmission; RF reception; Detection sensitivity

1. Introduction

In vivo ^{31}P magnetic resonance (MR) spectroscopy (MRS) imaging technique provides a valuable tool for noninvasively studying cerebral high-energy phosphate metabolism, neuroenergetics, intracellular redox state of nicotinamide adenine dinucleotide (NAD), phospholipid metabolism and brain function [1,2]. However, low concentrations (from sub-millimolar to few millimolar) of the phosphate metabolites in the human brains pose a daunting challenge to achieve adequate spatial and temporal resolutions, particularly for ^{31}P chemical shift imaging (CSI) application, in addressing biomedical questions.

Up to now, the conventional paradigm for gaining detection sensitivity and improving spectral resolution is to increase the static magnetic field strength (B_0). The signal-to-noise ratio (SNR) of *in vivo* ^{31}P MRS in the brain has an approximately linear dependence on B_0. For instance, the apparent SNR of the phosphocreatine (PCr) signal measured by *in vivo* ^{31}P MRS increased ~60% at 7.0 Tesla (T) compared to 4.0 T in human brain [3], and ~70% at 16.4 T compared to 9.4 T in rodent brain [4]. With this paradigm, high field MR technology has significantly improved spectral resolution and SNR, which, in turn, improves spatial and/or temporal resolution [3–7]. However, building a stronger magnet for further improvement of SNR for human application becomes very challenging due to technology limitation as well as high cost. Another challenge associated with higher magnetic field is the elevated radiofrequency (RF) power deposition or a specific absorption rate (SAR), which is a safety concern for the ^{1}H MRI applications demanding high RF pulse duty cycle at 7.0 T. Interestingly, X-nuclear MRS requires even higher RF transmitter power for achieving the same RF pulse flip angle as the ^{1}H MRS because of its lower gyromagnetic ratio (γ) [8,9], which might pose similar SAR concern and RF engineering challenges as ^{1}H MRI at ultrahigh field.

In seeking of alternative solutions for these challenges, the approach that incorporates high dielectric constant (HDC) materials into RF coils has demonstrated new utility to effectively improve RF magnetic transmit field ($|B_1^+|$) efficiency and RF reception field ($|B_1^-|$), thus, detection sensitivity across a broad frequency range [10–16]. The theoretical basis for enhancement of the HDC material on the RF field is that the induced displacement current in the HDC materials acts as a secondary RF field source for enhancing both B_1^+ and B_1^- (see details in Methods). The effect of this approach has initially been demonstrated for ^{1}H MRS at 7.0 T using water-based slurries with a permittivity of approximately 110 [11]. Since the displacement current is proportional to permittivity of the material, materials with higher permittivity may be considered for achieving a greater enhancement effect for low-γ nuclear applications. However, the exploration of the HDC technology for MR applications have been limited to the dielectric materials with relatively low permittivities in the range of few hundreds, it would be interesting to exploit and investigate higher or ultrahigh dielectric

constant (uHDC) materials for substantially improving X-nuclear MRS operated at relatively low Larmor frequency [12].

Several approaches have been attempted to increase higher permittivity with water-based mixtures of powders or beads of dielectric materials [10]. To increase permittivity, a transition to high-density composite dielectric materials is necessary. Most recently, we have demonstrated that for proton imaging at 3.0 T, a several-fold reduction of transmission power and significant SNR improvement could be achieved using monolithic ceramics with ultrahigh permittivity (on the order of thousands) and low loss [17,18]. Since ^{31}P resonance frequency at 7 T (120 MHz) is close to that of ^{1}H at 3.0 (125 MHz), utilizing the similar uHDC materials at 7 T could offer a viable solution for the conundrum of high SAR and low SNR for *in vivo* ^{31}P MRS applications.

In this study, we conducted a study using uHDC (permittivity ≈ 1200) ceramic blocks incorporated with an RF volume coil at 7.0 T for synergistically improving detection sensitivity and reducing the required RF power for *in vivo* ^{31}P MRS imaging application in human.

2. Methods

2.1. Theory

A simple principle underlying the HDC technique can be shown by Ampere's circuital law with Maxwell addition,

$$\oint_L B_1 \cdot dl = \mu \iint_A \sigma E \cdot dS + \mu \frac{\partial}{\partial t} \iint_A \varepsilon_0 \varepsilon_r E \cdot dS \quad (1)$$

where B_1 is the magnetic flux density of the RF field, E is the electric field strength, μ is permeability, σ is electrical conductivity, ε_r is relative electric permittivity or *dielectric constant* and ε_0 is electric permittivity of free space. The first and second terms on the right side of Eq. (1) are the *conductive* and *displacement current* densities, respectively. This equation states that these two types of currents are the sources attributed to the magnetic field B_1 which is highly relevant to MRI and MRS applications. Conventionally, most of the RF coil engineering community has focused on the first term in developing the RF coil techniques: *i.e.*, how to induce the magnetic field efficiently with the conductive current in the RF coil. The displacement current is relatively small in free space where $\varepsilon_r \approx 1$ at the RF operation frequency regime for most MRI and MRS applications, for instance, 125 MHz for ^{1}H MRI at 3 T and 120 MHz for ^{31}P MRS at 7.0 T. Since the displacement current is proportional to ε_r, uHDC material with $\varepsilon_r > 1000$-fold of air would largely enhance the contribution from the second term in Eq. (1), and generate greater magnetic flux density within and through the uHDC materials. The B_1 flux produced by the displacement current in the uHDC material extends into the nearby space. The superposition of the B_1 fields produced by the current in the RF coil and that in the uHDC material establishes enhanced B_1 distribution with greatly focused field in the sample close to the uHDC materials. Thus,

insertion of the uHDC material between RF coil and sample can result in enhancement of both B_1^+ and B_1^- of the RF coil in the region of interest (ROI) inside the sample, leading to improvements in the RF transmission efficiency and signal detection sensitivity concurrently. More details in regards the theoretical analysis and modeling simulation of B_1^+ and B_1^- changes induced by the use of uHDC block(s) have been described in the literature [12,14, 15].

One caveat is that the theoretical description above is only valid under non-resonance condition within the uHDC blocks. It is known that intrinsic resonances could exist in these monolithic dielectric materials with regular geometric shapes under non-optimal operation frequency, and the theoretical analysis under these conditions must be treated differently, which is beyond the scope of current study.

2.2. uHDC material

Four rectangular ceramic uHDC blocks (10 cm × 8 cm, and 2 cm thickness) were made of ferroelectric material of lead zirconate titanate (PZT: $Pb(Zr, Ti)O_3$) ceramics (HyQ Research Solutions, LLC, State College, PA), which has an ultrahigh effective dielectric constant value ($\varepsilon_{eff} \approx 1200$) suitable for the Larmor frequency of ^{31}P MRS (120 MHz) operated at 7.0 T. The loss tangent value of the uHDC blocks was 0.05 in the operation frequency range of 120–125 MHz [19].

2.3. ^{31}P MRS measurement

All ^{31}P MRS experiments were carried out on a Siemenswhole-body/90-cm bore 7.0 T human scanner (MAGNETOM, Erlangen, German) with a ^{31}P—^{1}H dual-nuclei transverse electromagnetic (TEM) volume coil (inner diameter = 28 cm, coil length = 10 cm) consisting of eight RF coil elements for each ^{1}H and ^{31}P coil channel operated at quadrature RF power mode [20,21]. Both ^{31}P and ^{1}H coil channels were tuned and matched separately for each measurement with or without the use of uHDC blocks. All quantitative comparison of B_1 fields for ^{31}P MRS imaging tests was based on three-dimensional (3D) CSI using the Fourier Series Window (FSW) technique [20,22]. The experimental protocol was consisted of paired acquisition of two data sets: with and without uHDC blocks, for the B_1 comparisons in each phantom or human measurement. A care was taken to place the object sample in the same position within the RF coil for paired MRS acquisitions.

A ^{31}P phantom study was performed using a rectangular bottle (14.6 cm × 8.6 cm × 8.6 cm) filled with inorganic phosphate (Pi: 50 mM), sodium chloride (50 mM), and gadolinium contrast agent (0.05 mM) for shortening the longitudinal relaxation time (T_1) of Pi to ~300 ms at 7 T. Four uHDC blocks were positioned on the top, bottom, left and right side of the rectangular bottle, and parallel to the B_0 direction. Multiple 3D ^{31}P CSI data sets were acquired under full relaxation condition with the following parameters: repetition time (TR) = 2 s, RF (hard) pulse width = 750 μs, 3D phase encode steps = 9 × 9 × 7, spectral bandwidth = 5 kHz, field of view (FOV) = 15 × 15 × 20 cm^3, number of complex data points of FID=1024, various RF pulse flip angles by adjusting RF transmitter power voltage, and number of signal average = 1.

In vivo ^{31}P MRS experiments were performed on healthy volunteers and the study protocol was approved by the Institutional Review Board of the University of Minnesota. Four uHDC blocks were positioned on the top, bottom, left and right side of the subject's leg to cover the calf muscle. A series of the 3D ^{31}P CSI data were acquired under partially saturated relaxation condition with variable RF transmitter power voltages covering an Ernst flip angle (FA = 68°) for PCr resonance [23] (TR = 1.5 s, 3D phase encode steps = 9 × 9 × 7, spectral bandwidth = 5 kHz, FOV = 15 × 15 × 20 cm^3, number of complex data points = 800, RF hard pulse width = 750 μs, and number of signal average = 1). The nominal voxel size of 3D CSI was 6.2 ml, and total acquisition time was 8 min for collecting each CSI volume.

Additionally, *in vivo* 3D ^{31}P CSI data with the same acquisition parameters were acquired using a ^{31}P—^{1}H dual-nuclei RF probe with a single-loop ^{31}P transmit-receive surface coil (diameter=6 cm) without using the uHDC blocks to compare its detection sensitivity with that of TEM volume coil plus the uHDC blocks.

Post-processing of the ^{31}P MR spectra included zero-filling of FIDs to 2048 data points. Spectrum analysis was performed using a Lorentzian-curve fitting with AMARES fitting algorithms [24] and the spectral noise level was calculated using a standard deviation (SD) of spectral baseline in the chemical shift regions in the absence of ^{31}P signals.

2.4. B_1 maps

The Pi and PCr signal was used to quantify B_1 maps for phantom and *in vivo* measurements, respectively. The relative magnitude of B_1^+ is inversely proportional to the RF transmitter voltage for reaching a 90° RF pulse flip angle ($V_{90°}$), and the relative magnitude of B_1^- is proportional to the maximum ^{31}P MRS signal reached at 90° RF pulse flip angle (FA) under fully relaxed acquisition condition ($S_{90°}$). These relationships were employed to generate the B_1^+ and B_1^- maps (in the transverse imaging orientation) based on a series of 3D CSI data sets acquired with multiple RF transmitter power voltages. As described previously [25, 26], the voxel-based B_1 field maps can be regressed and determined using the following equations:

$$S \propto \rho \cdot B_1^- \cdot SF \cdot sin(FA) \quad (2)$$

$$FA = \gamma \cdot \tau \cdot |B_1^+| \cdot V \quad (3)$$

$$SF = \frac{1 - exp\left(-\frac{TR}{T_1}\right)}{1 - cos(FA) \cdot exp\left(-\frac{TR}{T_1}\right)} \quad (4)$$

where S is the measured signal of ^{31}P MRS, ρ is the spin density, SF is a saturation factor and it equals to 1 under fully relaxed acquisition condition, τ is the time duration of reference RF pulse, V is a RF transmitter voltage. T_1 value used for PCr in the human calf muscle at 7 T was 4 s [27]. Based on the fact that the signal depends sinusoidally on B_1^+ and linearly on B_1^-, B_1 maps were estimated using a nonlinear curve fitting algorithm. All data processing was performed using a custom-built program in Matlab software (v14.0, Mathworks) based on Eqs. (2) to (4).

3. Results

Fig. 1 illustrates the experimental setup with (1A) and without (1B) the placement of the four uHDC blocks and the corresponding ^{31}P CSI spectra (1C and 1D) using the rectangular bottle phantom filled with 50 mM Pi. The Pi signal intensities show a typical distribution from a RF volume coil at 7.0 T with relatively high signal intensities in the central area of the phantom. Fig. 1E demonstrates the regression results of the Pi signal intensity *vs.* RF transmitter power voltage from the two voxels selected in the same position in the phantom as indicated in 1C and 1D under the two conditions. As shown in Fig. 1E, the RF transmitter power voltage for reaching a nominal 90° flip angle was 211 and 92 V without and with uHDC blocks, respectively, indicating a ~130% increase in B_1^+ (or approximately 5 times reduction in the required RF power for reaching the same RF flip angle), the corresponding maximum reception signal at 90° FA (proportional to B_1^-) also increased by ~140% in the same voxel using the uHDC blocks.

Fig. 2 illustrates the configuration of four uHDC blocks placement around the phantom (2A), and significant enhancements of both B_1^- (2B–D) and B_1^+ (2E–G) up to 3-fold inside the phantom surrounded by the four uHDC blocks as compared to that without the blocks.

Fig. 3A shows the experimental setup for conducting *in vivo* ^{31}P MRS study of human calf muscle with the uHDC blocks placed on four sides of the leg. Figs. 3B–C display representative 3D ^{31}P CSI data (one central CSI slice) of the human calf muscle with (3B) and without (3C) the use of uHDC blocks. Similar to the phantom experiment results, *in vivo* ^{31}P CSI spectra show a similar pattern of signal distribution: relatively higher signal intensities in the center and relatively lower in the periphery regions. Compared to the control ^{31}P signals without the uHDC blocks, the use of the uHDC blocks led to a large B_1 improvement reflected by SNR enhancement and reduction of the RF transmitter voltage (from 141 to 63 V) required for achieving the similar flip angle; the B_1^+ efficiency and the average SNR (proportional to B_1^-) were improved up to a factor of 2–3 as shown in the B_1 ratio maps in Figs. 4 and 5 from two representative subjects. Fig. 4*H* demonstrates one example for determining the relative magnitudes of B_1^- and B_1^+ fields in a representative voxel of human calf muscle under partially relaxed acquisition condition. The signal dependence on the RF transmitter voltage did not obey the sinusoidal function, thus,

requiring the consideration of saturation correction factor using the term of SF in Eq. (2) for regression.

As shown in Fig. 3D, the sensitivity enhancement by the uHDC blocks in conjunction with the ^{31}P RF volume coil was further evaluated by comparing with that of ^{31}P single-loop surface coil (with *no* uHDC block), at approximately the same location near the superficial region of the subject's calf muscle. Strikingly, the measured SNR of the RF volume coil incorporated with the uHDC block was even slightly higher than that detected by the small surface coil.

4. Discussion

In the present work, the phantom and *in vivo* ^{31}P MRS imaging measurements clearly demonstrate that incorporation of the uHDC blocks into an RF volume coil could result in >100% SNR increase and less than half of the RF transmitter voltage required for achieving a given flip angle as compared to that without the uHDC materials. In a recent study, it has been shown that using uHDC materials can enhance B_1 for ^{1}H MRI applications at 3.0 T [16]. Although the present study is a translation of the similar uHDC technique to ^{31}P MRS application at 7.0 T, its impacts should be profound for low-γ X-nuclear MRS imaging applications because the low inherent SNR and high demanding of RF transmitter voltage have severely limited *in vivo* low-γ MRS applications. Overcoming these limitations will enable many potential applications that are previously unachievable. For example, ^{31}P and ^{17}O are two biologically important nuclei for studying brain energetics [1,2,20, 28–30]. The detection sensitivities of ^{31}P and ^{17}O relative to ^{1}H (assumed as 1) are 6.63×10^{-2} and 1.08×10^{-5}, respectively. Thus, considering the vast concentration differences between ^{1}H water and ^{31}P phosphate metabolites (~8000 times) or ^{17}O natural abundant water (~2700 times), a high magnetic field strength is generally required for obtaining adequate SNR within the allowable data acquisition time for *in vivo* ^{31}P or ^{17}O MRS study. On the RF transmission side, the voltage for a given pulse flip angle should be increased inversely proportional to the γ ratio of X-nucleus to ^{1}H, if assuming the same RF coil efficiency for the two nuclei or operation frequencies. For instance, the RF transmitter voltage required for ^{31}P would be about 2.5 times of ^{1}H at the same field strength. As demonstrated herein, the application of the four uHDC blocks in the present work improved the B_1^+ efficiency by >100% that substantially reduced RF power demand. Thus, the enhancements observed for *in vivo* ^{31}P MRS imaging brought by the uHDC technique open up an avenue for other low γ-nucleus MRS applications with even lower Larmor frequency such as ^{17}O, ^{2}H and ^{23}Na [9].

Conventionally, the SNR of *in vivo* ^{31}P MRS could be improved significantly by using a small local RF surface coil rather than a large RF volume coil due to the proximity between the RF surface coil and the object of interest. However, such improvement is only in the superficial region of object close to the coil. Strikingly, the ^{31}P spectra acquired from the RF volume coil with uHDC blocks provided equivalent or even slightly better sensitivity for the voxel selected from the optimal location for the surface coil with a similar RF transmit power. In addition, although the strongest B_1 improvement was in the voxels near the uHDC blocks, there was an overall B_1 enhancement in a large number of CSI voxels beyond the

superficial region of object. A >100% SNR gain for detecting the muscle PCr metabolite *in vivo* with the uHDC technique at 7 T could provide an equivalent SNR performance expected at >14 T [4], but without the concern of increasing SAR. Thus, the uHDC technique can lead to a novel engineering solution that will improve MR detection sensitivity and SNR beyond the limitation set by the static magnetic field strength [13,31]. Moreover, the uHDC technology provides a simple, cost-effective approach to substantially improve SNR for the X-nucleus MRS applications without alterations of hardware or software.

This study demonstrates a proof of concept in utilizing uHDC material for boosting detection sensitivity of X-nucleus MRS beyond the limit set by B_0 strength. The enhancements demonstrated in this work were achieved under sub-optimal conditions. Several technical challenges must be resolved in order to implement the uHDC technology for broad and routine human studies. First, the permittivity and geometry (size and shape) of uHDC materials should be optimized along with given RF coil designs (volume coil, surface coil or phase array coils) and conformed with the object of interest. Second, since the suitable permittivity for each nuclear species is frequency dependent, uHDC material suitable for ^{31}P studies could perturb the B_1 field for ^{1}H-application in the sample, which makes it difficult to acquire high quality ^{1}H anatomical images or perform optimal B_0 shimming. The B_1 field enhanced by the uHDC materials with limited volume coverage can also make the RF transmission field inhomogeneous, which could lead to large variation in the distribution of RF pulse flip angle and MR signal in space. Thus, significant engineering work must be carried out in order to make the uHDC technology widely adopted for *in vivo* X-nucleus MR applications.

5. Conclusion

Our experimental results from phantom and *in vivo* human calf muscle at 7.0 T demonstrate that incorporating uHDC materials with RF coil can provide an efficient, cost-effective engineering solution for substantially boosting SNR and concurrently reducing required RF transmit power for human application of X-nuclei MRS imaging. The successful development of the uHDC technology could exceed the detection sensitivity limit set by the given static field strength and, therefore, provide enormous benefits for high-field ^{31}P MRS applications.

Acknowledgments

This work was partly supported by NIH Grants R24 MH106049 and R24 MH106049 S1, RO1 NS057560, NS070839 and MH111413, S10 RR026783, P41 EB015894, P30 NS076408; a grant from Penn State Hershey Neuroscience Institute, and the AHC Faculty Research Development (FRD) grant from the University of Minnesota. The authors thank Drs. Kamil Ugurbil and Gregor Adriany for technical support and scientific discussion.

Abbreviations

MRS	magnetic resonance spectroscopy
CSI	chemical shift imaging

FSW	Fourier series window
RF	radiofrequency
SNR	signal-to-noise ratio
HDC	high dielectric constant
uHDC	ultrahigh dielectric constant
B_1^+	RF magnetic transmit field
B_1^-	RF magnetic reception field
E	electric field
NAD	nicotinamide adenine dinucleotide
$\mathbf{B_0}$	static magnetic field strength
PCr	phosphocreatine
SAR	specific absorption rate
$\boldsymbol{\gamma}$	gyromagnetic ratio
$\boldsymbol{\varepsilon_r}$	relative permittivity
TEM	transverse electromagnetic
T	tesla

References

1. Zhu XH, et al. In vivo NAD assay reveals the intracellular NAD contents and redox state in healthy human brain and their age dependences. Proc Natl Acad Sci U S A. 2015; 112(9):2876–81. [PubMed: 25730862]
2. Du F, et al. Tightly coupled brain activity and cerebral ATP metabolic rate. Proc Natl Acad Sci U S A. 2008; 105(17):6409–14. [PubMed: 18443293]
3. Qiao H, et al. In vivo ^{31}P MRS of human brain at high/ultrahigh fields: a quantitative comparison of NMR detection sensitivity and spectral resolution between 4 T and 7 T. Magn Reson Imaging. 2006; 24(10):1281–6. [PubMed: 17145398]
4. Lu M, Chen W, Zhu XH. Field dependence study of in vivo brain ^{31}P MRS up to 16. 4 T. NMR Biomed. 2014; 27(9):1135–41. [PubMed: 25070004]
5. Terpstra M, et al. Test-retest reproducibility of neurochemical profiles with shortecho, single-voxel MR spectroscopy at 3T and 7T. Magn Reson Med. 2016; 76(4):1083–91. [PubMed: 26502373]
6. Tkac I, et al. In vivo ^{1}H NMR spectroscopy of the human brain at high magnetic fields: metabolite quantification at 4T vs. 7T. Magn Reson Med. 2009; 62(4):868–79. [PubMed: 19591201]
7. Wijtenburg SA, et al. Reproducibility of brain spectroscopy at 7T using conventional localization and spectral editing techniques. J Magn Reson Imaging. 2013; 38(2):460–7. [PubMed: 23292856]
8. Perman WH, et al. Methodology of in vivo human sodium MR imaging at 1. 5 T. Radiology. 1986; 160(3):811–20. [PubMed: 3737922]

9. Wiesner, HM. Quantitative study of TX/RX-efficiency of X-nuclear MRS/MRI at high/ultrahigh field. Proceeding of Annual Meeting of International Society for Magnetic Resonance in Medicine (ISMRM); 2014; Milan, Italy.
10. Luo W, et al. Permittivity and performance of dielectric pads with sintered ceramic beads in MRI: early experiments and simulations at 3 T. Magn Reson Med. 2013; 70(1):269–75. [PubMed: 22890908]
11. Snaar JE, et al. Improvements in high-field localized MRS of the medial temporal lobe in humans using new deformable high-dielectric materials. NMR Biomed. 2011; 24(7):873–9. [PubMed: 21834010]
12. Webb AG. Dielectric materials in magnetic resonance. Concepts in Magnetic Resonance Part A. 2011; 38A(4):148–84.
13. Yang QX, et al. Manipulation of image intensity distribution at 7. 0 T: passive RF shimming and focusing with dielectric materials. J Magn Reson Imaging. 2006; 24(1):197–202. [PubMed: 16755543]
14. Yang QX, et al. Radiofrequency field enhancement with high dielectric constant (HDC) pads in a receive array coil at 3. 0T. J Magn Reson Imaging. 2013; 38(2):435–40. [PubMed: 23293090]
15. Yang QX, et al. Reducing SAR and enhancing cerebral signal-to-noise ratio with high permittivity padding at 3 T. Magn Reson Med. 2011; 65(2):358–62. [PubMed: 21264928]
16. Rupprecht, S. Drastic enhancement and manipulation of RF field with ultra high dielectric constant (uHDC) material at 3T. Proceeding of Annual Meeting of International Society for Magnetic Resonance in Medicine (ISMRM); 2013; Salt Lake City, UT, USA.
17. Rupprecht, S., et al. Signal-to-noise ratio improvement for MR proton spectroscopy at 3T using an ultra-high dielectric constant (uHDC) material sleeve. Proceeding of Annual Meeting of International Society for Magnetic Resonance in Medicine (ISMRM); 2014; Milan, Italy.
18. Rupprecht, S., et al. Drastic enhancement and manipulation of RF field with ultra high dielectric constant (uHDC) material at 3T. Proceeding of Annual Meeting of International Society for Magnetic Resonance in Medicine (ISMRM); 2013; Salt Lake City, UT, USA.
19. Bottger U, Arlt G. Dielectric microwave dispersion in PZT ceramics. Ferroelectrics. 1992; 127:95–100.
20. Zhu XH, et al. Quantitative imaging of energy expenditure in human brain. Neuroimage. 2012; 60(4):2107–17. [PubMed: 22487547]
21. Zhang, XL. A circular-polarized double-tuned (^{31}P and ^{1}H) TEM coil for human head MRI/MRS at 7T. Proceeding of Annual Meeting of International Society for Magnetic Resonance in Medicine (ISMRM); 2003; Toronto, Canada.
22. Garwood M, Schleich T, Ugurbil K. The Fourier-series window method for spatially localized Nmr-spectroscopy - implementation with composite pulses and multiple coils. Ann N Y Acad Sci. 1987; 508:512–5.
23. Jordan CD, et al. Musculoskeletal MRI at 3.0 T and 7. 0 T: a comparison of relaxation times and image contrast. Eur J Radiol. 2013; 82(5):734–9. [PubMed: 22172536]
24. Vanhamme L, van den Boogaart A, Van Huffel S. Improved method for accurate and efficient quantification of MRS data with use of prior knowledge. J Magn Reson. 1997; 129(1):35–43. [PubMed: 9405214]
25. Collins CM, Smith MB. Signal-to-noise ratio and absorbed power as functions of main magnetic field strength, and definition of “90 degrees” RF pulse for the head in the birdcage coil. Magn Reson Med. 2001; 45(4):684–91. [PubMed: 11283997]
26. Hoult DI. The principle of reciprocity in signal strength calculations—a mathematical guide. Concepts in Magnetic Resonance. 2000; 12(4):173–87.
27. Bogner W, et al. Assessment of ^{31}P relaxation times in the human calf muscle: a comparison between 3 T and 7 T in vivo. Magn Reson Med. 2009; 62(3):574–82. [PubMed: 19526487]
28. Zhu, XH., Chen, W. In vivo ^{17}O MRS imaging - quantitative assessment of regional oxygen consumption and perfusion rates in living brain. Anal Biochem. 2016. http://dx.doi.org/10.1016/j.ab.2016.08.026

29. Zhu, XH., et al. Study of brain bioenergetics and function using in vivo MRS. In: Kamil Ugurbil, KU., Lawrence, Berliner, editors. Biological magnetic resonance: fMRI: from nuclear spins to brain function. New York: Springer; 2015. p. 819-64.

30. Zhu XH, et al. Development of ^{17}O NMR approach for fast imaging of cerebral metabolic rate of oxygen in rat brain at high field. Proc Natl Acad Sci U S A. 2002; 99(20):13194–9. [PubMed: 12242341]

31. Caserta J, Beck BL, Fitzsimmons JR. Reduction of wave phenomena in high-field MRI experiments using absorbing layers. J Magn Reson. 2004; 169(2):187–95. [PubMed: 15261613]

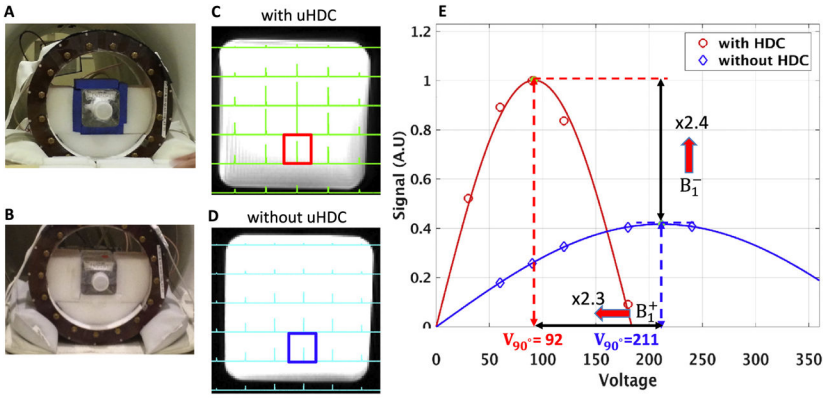

Fig. 1.

Demonstration of ^{31}P CSI improvements by using the uHDC technique based on phantom tests. The left panel exhibits experimental setup of the uHDC blocks placed around the phantom (**A**), and without blocks but keep the phantom at the same position inside the TEM RF volume coil (**B**). Middle column displays the 2D CSI slices (in the axial plane) selected from 3D CSI dataset with the uHDC blocks using a RF pulse reference voltage of 80 V (**C**), and without the uHDC blocks using a reference voltage of 160 V (**D**). (**E**) Estimation of B_1 improvements in the highlighted voxels (in **C** and **D**) using a sinusoidal curve fitting algorithm. It shows that B_1^- increased 140% and B_1^+ increased 130% for the representative voxel.

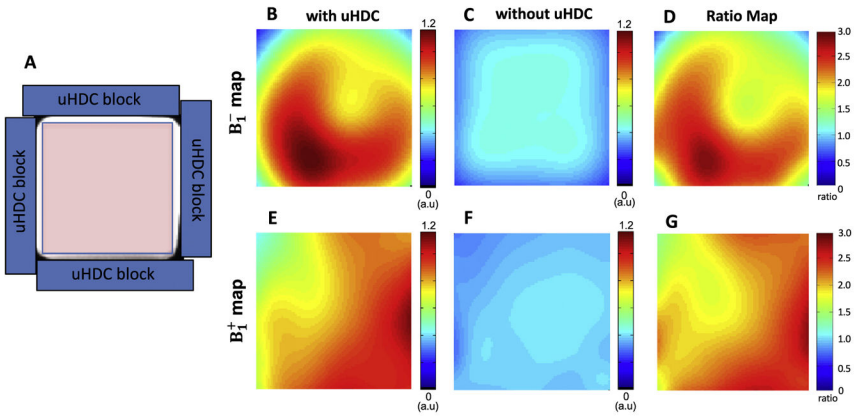

Fig. 2.

Comparison of ^{31}P B_1 maps (in the axial plane) within the rectangular bottle phantom (left panel). (**A**) The configuration of uHDC blocks (blue bars) placed around the phantom. The B_1 maps (the scale bar is an arbitrary unit, a.u.) with the uHDC blocks (**B**, **E**) shows large enhancement of B_1 efficiency compared to without the uHDC blocks (**C**, **F**). The B_1 ratio maps (**D**, **G**) represent B_1 with uHDC over B_1 without uHDC, indicating significant enhancement that reached over 200% improvement in some image areas.

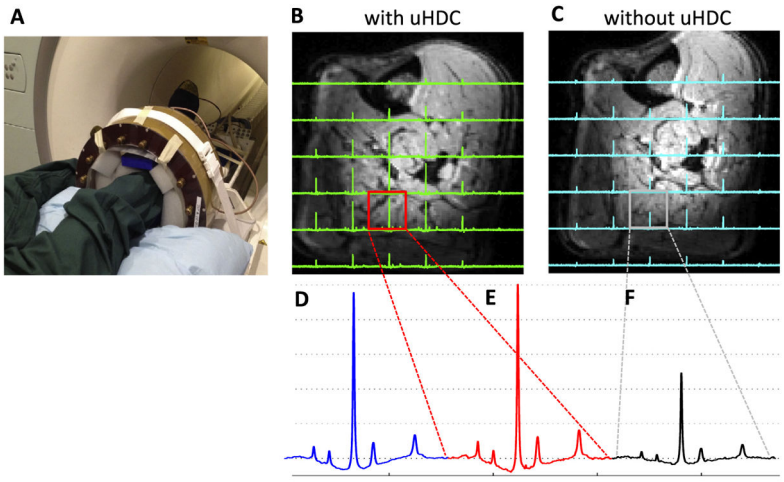

Fig. 3.

(**A**) Photograph of experimental setup for the *in vivo* ^{31}P MRS study of the human calf muscle with the placement of four uHDC blocks around the subject's leg. *In vivo* ^{31}P CSI profiles with the uHDC blocks at a RF pulse reference voltage of 63 V (**B**), and without the blocks at a reference voltage of 141 V (**C**). (**D**) Comparison of *in vivo* ^{31}P spectra acquired using the small ^{31}P surface coil at a reference voltage of 60 V, and the ^{31}P volume coil with (**E**) and without the uHDC blocks (**F**).

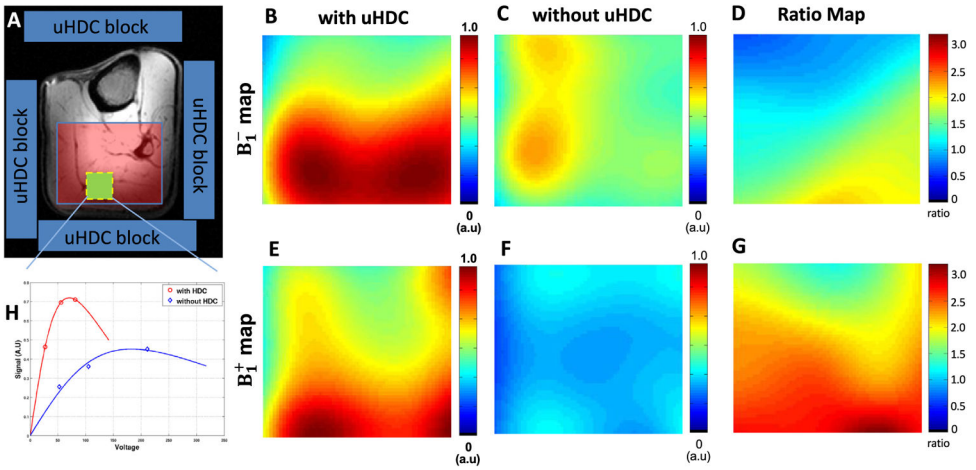

Fig. 4.

Comparison of ^{31}P B_1 maps (in the axial plane) of the selected human calf muscle (left panel) from one representative subject. (**A**) shows the schematic placement of 4 uHDC blocks (blue) around the leg. The B_1 maps (the scale bar is in an arbitrary unit, a.u) with the uHDC blocks (**B**, **E**) show large enhancement of B_1 efficiency as compared to the case without the uHDC blocks (**C**, **F**). The B_1 ratio maps (**D**, **E**) represent theB_1 with uHDC over B_1 without uHDC. (**H**) shows the calibration of the B_1 values of the highlighted voxel (green box in **A**) using a nonlinear curve fitting algorithm with saturation effect correction.

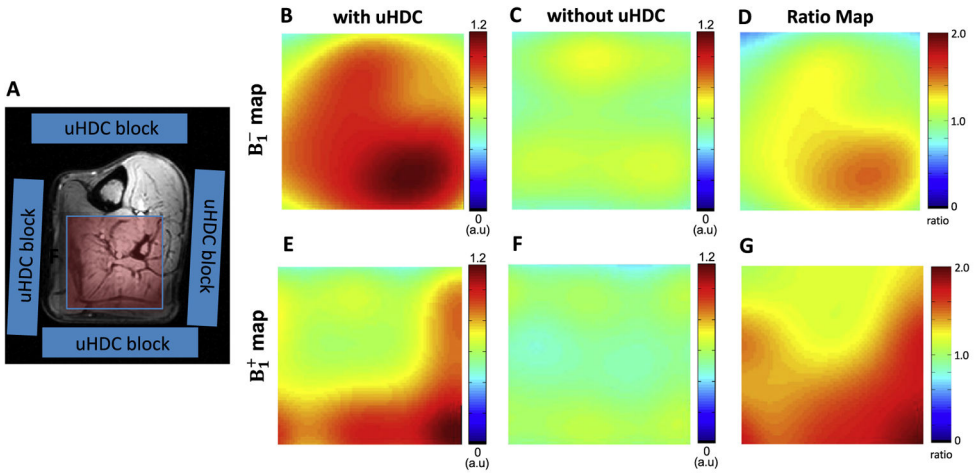

Fig. 5.

Comparison of ^{31}P B_1 maps (in the axial plane) of selected human calf muscle (left panel) in another subject. (**A**) shows the schematic placement of 4 uHDC blocks (blue) around the leg. The B_1 maps (the scale bar is in an arbitrary unit, a.u.) with the uHDC blocks (**B**, **E**) show large enhancement of B_1 efficiency compared to the case without the uHDC blocks (**C**, **F**). The B_1 ratio maps (**D**, **E**) represent the B_1 with uHDC over B_1 without uHDC.